

HIGH RESOLUTION CHANDRA HETG AND RXTE OBSERVATIONS OF GRS 1915+105 : A HOT DISK ATMOSPHERE & COLD GAS ENRICHED IN IRON AND SILICON

JULIA C. LEE¹, CHRISTOPHER S. REYNOLDS^{2,3}, RONALD REMILLARD¹, NORBERT S. SCHULZ¹,
 ERIC G. BLACKMAN⁴, ANDREW C. FABIAN⁵,

Accepted for publication in The Astrophysical Journal, 2001 November 6

ABSTRACT

The time-averaged 30 ks *Chandra* AO1 HETGS observation of the micro-quasar GRS 1915+105 in the low hard state reveals for the first time in this source neutral K absorption edges from iron, silicon, magnesium, and sulphur. Ionized resonance (*r*) absorption from H- and He- like species of Fe (XXV, XXVI) and possibly Ca XX are also seen as well as possible emission from neutral Fe K α and ionized Fe XXV (forbidden, or the resonance emission component of a P-Cygni profile). We report the tentative detection of the first astrophysical signature of XAFS in the photoelectric edge of Si (and possibly Fe and Mg), attributed to material in grains. The large column densities measured from the neutral edges reveal anomalous Si and Fe abundances, and illustrate the importance of high resolution X-ray measurements for assessing material which surrounds bright X-ray sources, especially if depletion onto grains plays a prominent role. Scenarios for which the anomalous abundances can be attributed to surrounding cold material associated with GRS 1915+105 and/or that the enrichment may signify either a highly unusual supernova/hypernova, or external supernova activity local to the binary are discussed. We attribute the ionized features to a hot disk, disk-wind, or corona environment. Based on H- and He-like Fe (XXV, XXVI), we estimate constraints on the ionization parameter ($\log \xi \gtrsim 4.15$), temperature ($T > 2.4 \times 10^6$ K), and hydrogen equivalent number density ($n \gtrsim 10^{12} \text{ cm}^{-3}$) for this region. Variability studies with the simultaneous *RXTE* data show that the light curve count rate tracks the changes in the disk blackbody as well as the power-law flux, with the most significant variations observed in the former. Similar studies of the *Chandra* spectra show spectral changes which also track the behavior of the light curve, and may point to changes in both the ionizing flux and density of the absorber. A 3.69 Hz QPO and weak first harmonic is seen in the *RXTE* data.

Subject headings: binary; micro-quasars; general; X-ray; general; individual GRS 1915+105

1. INTRODUCTION

The Galactic X-ray transient GRS 1915+105 is an extremely energetic X-ray binary that has been studied extensively in multiple wavebands which include radio, infrared and X-rays (e.g. see review by Mirabel & Rodríguez 1999). Since its discovery by *Granat*/WATCH in 1992 (Castro-Tirado et al. 1992), it has shown repeated flares separated by intervals in a “low-hard” state. In the X-ray band, the overall variability of GRS 1915+105 is extremely complex, with a luminosity which varies between a few $\times 10^{37}$ – few $\times 10^{39} \text{ erg s}^{-1}$, making it one of the most energetic objects known in the Galaxy. Many of these variations can be understood in terms of instabilities that switch the origin of radiant energy between two components: the accretion disk and the X-ray power-law (Muno, Morgan, & Remillard 1999). Recent observations in the near-infrared H & K band with the VLT reveal the donor to be a K-M III giant (Greiner et al., 2001a) with a 33 day binary period and a radial velocity curve interpreted to suggest a compact object of $\sim 14M_{\odot}$ (Greiner et al, 2001b). This indicates that GRS 1915+105 belongs to the class of dynamically established black hole binaries.

One of the most remarkable aspects of this system is that X-ray flares are sometimes followed by superluminal ejection events seen in radio images (Mirabel & Rodríguez 1994;

Fender et al. 1999) — the inferred velocity of the knots in the bipolar jets is $v \sim 0.95c$ (i.e. a Lorentz factor of 3). Only a few sources in the Galaxy (e.g. GRO 1655–40 and XTE J1748–288) display such violent ejections, while other sources exhibit intervals of more constant radio emission associated with a steady jet (Mirabel & Rodríguez 1999). Both types of jet sources qualitatively resemble radio-loud active galactic nuclei (AGN) and are often called ‘micro-quasars’.

A key piece to the puzzle for understanding the physical environment of GRS 1915+105 is X-ray spectroscopy. *ASCA* observations of GRS 1915+105 have revealed striking structure within the (medium resolution) X-ray spectra. Based on observations in 1994–1995, Kotani et al. (2000) identified resonant absorption lines of Ca XX K α , Fe (XXV, XXVI) K α , as well as blends of absorption lines of Ni XXVII K α + Fe XXV K β and Ni XXVIII K α + Fe XXVI K β . However, *ASCA* is fundamentally limited in the extent to which it can clearly resolve absorption lines or detect emission components. Sufficient spectral resolution and energy coverage (such as presently possible with the *Chandra* high energy transmission grating) is particularly important for obtaining direct information on the line-of-sight velocity and velocity dispersion of the material. The absolute and relative equivalent widths of the lines can be used to determine the column density and ionization parameter of the accretion disk environment, and any disk wind. In this

¹Massachusetts Institute of Technology, Center for Space Research, 77 Massachusetts Ave. NE80, Cambridge, MA 02139.

²Dept. of Astronomy, University of Maryland, College Park MD 20742

³JILA - U. of Colorado, Campus Box 440, Boulder CO 80309; Hubble Research Fellow

⁴Dept. of Physics & Astronomy, University of Rochester, Rochester, NY 14627

⁵Institute of Astronomy, Cambridge University, Madingley Rd., Cambridge CB2 0HA U.K.

paper, we present primarily the prominent spectral features of the time averaged X-ray spectrum of GRS 1915+105 obtained with the high resolution gratings on-board *Chandra*. We assess the chemical abundances based on direct measurements of neutral K edges of Fe, S, Si, and Mg (§4). Measurements of ionized Fe features are used to assess the conditions of the accretion disk corona (§5). Variability is discussed in the context of *Chandra* and *RXTE* observations (§6). Preliminary results were presented in Lee et al. (2001a).

2. OBSERVATIONS

GRS 1915+105 was observed with the *Chandra* High Energy Transmission Grating (HETGS; Canizares et al., 2001, in preparation) on 2000 April 24 beginning at 01:35:49 (MJD: 51658.06654), with a total integration time ~ 31.4 ks. This corresponds to orbital phase ~ 0.8 according to the ephemeris quoted by Greiner (2001b), where phase zero (2000 May 02) is the time consistent with the blue-to-red crossing in the radial velocity. Simultaneous *RXTE* observations were performed with both the Proportional Counter Array (PCA, Jahoda et al., 1996) and High-Energy X-ray Timing Experiment (HEXTE, Rothschild et al., 1998) instruments.

Observations with the *RXTE* All-Sky Monitor over the time interval of 2000 April 21-28 indicate a relatively steady X-ray flux (16% rms variations) and a hard spectrum, with an average intensity of 0.4 Crab at 2-12 keV. Radio observations of GRS 1915+105 with the Greenbank Interferometer⁶ on 2000 April 24.54 indicate a flux of 20 ± 4 mJy at 2.25 GHz. The combined radio and X-ray properties place GRS 1915+105 in the "low-hard" state that is associated with the presence of a steady jet (Dhawan, Mirabel, & Rodriguez 2000; Munro, Remillard, & Morgan 2001).

Both the HETGS and the *RXTE* PCA instruments detect variations from GRS 1915+105 in the form of a smooth, 15% dip in the count rates that occurs midway through the observations (Fig. 4a, top 2 panels). The spectral variations are subtle, and so we first consider the average spectral features and then examine the dip in greater detail in §6.

2.1. The *Chandra* data & reduction

The *Chandra* HETGS is made up of the Medium Energy Grating (MEG) with a 2.5-31 Å (0.4-5 keV) bandpass, and High Energy Grating (HEG) with 1.2-14 Å (0.9-10 keV) bandpass. The peak resolving power ($E/\Delta E$) for the MEG and HEG is ~ 1000 . The resolution of the higher orders improves by a factor of n for the n th order, but the spectral bandpass and efficiency are reduced accordingly.

We observed GRS 1915+105 during a persistent phase of relatively low flux. Despite this, the observation suffered from photon pile-up. This is the phenomenon by which multiple photons fall on a single pixel during the same readout period. As a result, the on-board event detection algorithm interprets this as a single high energy photon event, and sums the multiple photon events to make a single pulse height. Pileup has the effect of depleting the photon spectrum, thereby decreasing the photon counting rate. Corrections for this effect will be discussed in §3.

Due to severe telemetry and photon pileup problems imposed by the large count rate of GRS 1915+105, the observation was performed using the *graded*⁷ telemetry mode, and a subarray

which reduced CCD framerate by a factor of ~ 2 . We additionally used a 'spatial window' to block out the 0th order image (this would have been completely piled-up, even during periods of low flux for the energetics of GRS 1915+105). However, because the 0th order position is crucial for defining an accurate wavelength scale, we calculate its position for our observation by finding the intersection of the dispersed MEG-HEG spectra with the 0th order readout trace. The accuracy of such a technique for the determination of the 0th order position is ~ 0.2 – 0.3 pixels, which translates respectively to a wavelength accuracy of 0.002 Å and 0.004 Å for the HEG and MEG 1st orders.

2.2. The *RXTE* data & reduction

We have analyzed the *RXTE* observations of 2000 April 24 that overlap the *Chandra* exposure of GRS 1915+105. At high time resolution, the PCA telemetry modes yielded 2 ms resolution for two energy channels that span 2–9 keV. We combined these channels and computed a power density spectrum, corrected for instrument deadtime and counting statistics (see Morgan, Remillard, & Greiner 1997). We then normalized the power spectrum to units of $(\text{rms fluctuations}/\text{mean})^2 \text{ Hz}^{-1}$ in the source, applying a small correction for the contribution of the diffuse X-ray background between 2–9 keV. The results show a QPO and a broadband power continuum typical of the low-hard state in GRS 1915+105 (e.g., Munro et al., 2001). The strongest QPO feature is at 3.69 Hz with an integrated amplitude of 8.5% and a weak first harmonic.

PCA and HEXTE spectra were derived from standard data modes that produce 128-channel PCA spectra (full bandwidth) every 16 s, and 64-channel HEXTE spectra (full bandwidth) at the instrument nodding period of 32 s. There were 3 PCUs in operation (units 0, 2, and 3) during the PCA observations, and our spectral analyses focus on results from PCUs 0 and 2 because of the superior performance of the associated calibration files (FTOOLS 5.6), as judged from the analysis of PCA observations of the Crab Nebula during late 2000 and early 2001.

3. THE SPECTRUM

The best fit continuum model which describes the *RXTE* data is a disk-blackbody plus a power-law component each modified by a hydrogen column of $5 \times 10^{22} \text{ cm}^{-2}$. The best fit color temperature of the disk is 1.4 keV ($\sim 1.6 \times 10^7$ K) with a normalization of $N_{\text{bb}} = 59$. (We note that the temperature deduced from this black body fit and that in the subsequent calculation of §5 based on the ratio of Fe XXV : Fe XXVI are not necessarily in conflict given that the DISKBB model is expected to overestimate the temperature by as much as a factor of 1.7 [Shimura & Takahara 1995], and the value given in §5 is a lower limit; however, the temperature measurements here and in §5 can also be probing independent components of the gas.) The average power-law component exhibits a photon index of $\Gamma \sim 2.4$ and a normalization of the power-law at 1 keV is $11.4 \text{ ph cm}^{-2} \text{ s}^{-1} \text{ keV}^{-1}$. The corresponding apparent (since there are losses due to low energy absorption) total 2–25 keV flux is $1.89 \times 10^{-8} \text{ erg cm}^{-2} \text{ s}^{-1}$. The implied (unabsorbed) bolometric fluxes are respectively $\sim 5.3 \times 10^{-9} \text{ erg cm}^{-2} \text{ s}^{-1}$ and $\sim 3.4 \times 10^{-8} \text{ erg cm}^{-2} \text{ s}^{-1}$ for the disk-blackbody and power-law (integrated from 1 keV to ∞) components, indicating that the

⁶<http://www.gb.nrao.edu/fgddocs/gbi/gbint.html>

⁷See *Chandra* Proposer's Observatory Guide at <http://asc.harvard.edu>

power-law component was the dominant emission mechanism during these observations. The absolute absorption corrected luminosity corresponding to the epoch of our observation is lower limit of $L_{bol} \approx L_X \approx 6.4 \times 10^{38} \text{ erg s}^{-1}$ at 12.5 kpc. We also assess the higher energy data afforded by *RXTE* HEXTE observations, and find that it is best fit with a broken power-law with the cutoff $E_{break} = 30 \text{ keV}$. The photon index below 30 keV is $\Gamma \sim 2.4$ (consistent with PCA measurements), and a steeper $\Gamma \sim 2.9$ spectrum above 30 keV. Since *RXTE* is better suited for constraining the continuum shape due to its wide band coverage, we apply this model to the *Chandra* data.

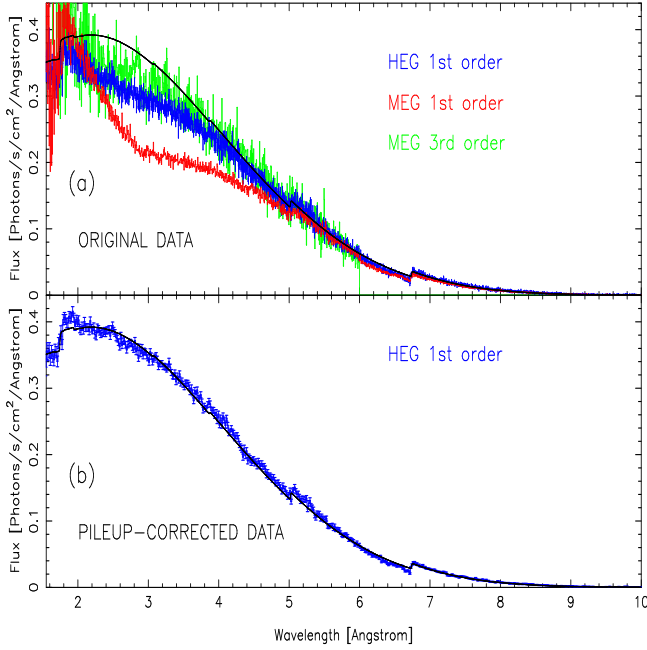


FIG. 1.— Best-fit *Chandra* continuum (black) based on best-fit *RXTE* continuum model over-plotted on the (a) non-pileup corrected *Chandra* HEG 1st order (blue), MEG 1st order (red), and MEG 3rd (red) order and (b) pileup corrected HEG 1st order (blue).

The overall shape of the continuum discussed above describes the *Chandra* data well (with the exception that the best fit power-law and power-law normalization are respectively $\Gamma \sim 2.1$ and $5.3 \text{ ph cm}^{-2} \text{ s}^{-1} \text{ keV}^{-1}$ for fits to the *Chandra* data), especially given the problems with pileup, which is responsible for $\sim 40\%$ of the 60% normalization difference between the *RXTE* and *Chandra* data. (Pileup will affect different parts of the spectrum by different amounts.) To illustrate, Fig. 1a shows the absorbed disk-blackbody plus power-law model over-plotted on the HEG 1st and MEG 1st & 3rd order data. Spectral deviations from the model in the MEG/HEG 1st order spectra at $\approx 2\text{--}5 \text{ Å}$ is due to pileup as a result of the high count rate of the source in this passband; instrumental pileup severely affects the 1st orders between $\approx 6.5\text{--}9 \text{ Å}$ since this is where the effective area of the HETGS peaks. The MEG 3rd order spectrum at $< 2 \text{ Å}$ is affected by both first order photon pileup at $\sim 5 \text{ Å}$ (i.e. MEG 3rd order pileup = $\lambda/\text{order} = 5\text{Å}/3$), and 0th order scattering. We extract a separate set of HEG and

MEG 1st order spectra to be used with the HETG pileup model as implemented in *ISIS*⁸ (see Davis 2001, Houck & DeNicola 2000). These data are extracted with a coarser (respectively for the HEG and MEG 1st orders $\sim 0.017\text{Å}$ and 0.033Å) binning to reflect the size of an ACIS event detection cell. The pileup corrected data shows a reduction from 60% to a few % in the overall normalization offset between *RXTE* and *Chandra* (Fig. 1b). We note that the broadband *RXTE* PCA flux is typically $\sim 15\text{--}25\%$ higher when compared against other X-ray missions (e.g. *ASCA*, *HEXTE*).

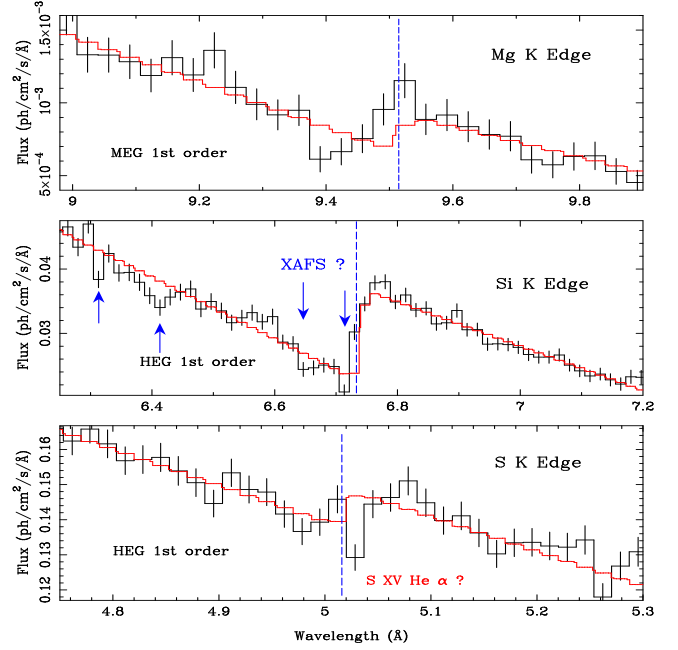


FIG. 2.— Photoelectric K-shell edges of S, Si and Mg. Overplotted are the respective best-fit models described in §2. Note the prominence of the Si edge, and possible XAFS structure. (The Fe K edge is shown in Fig. 3.)

4. PHOTOELECTRIC EDGES

We find evidence for prominent absorption edges due to K-shell Fe, S, Si, and Mg (Table 1, Figs. 2 & 3). Because the spectrum of GRS 1915+105 is complicated by ionized resonance features (e.g. Fig. 3), and possibly resonance structure due to X-ray absorption fine structure (XAFS), we derive τ by fitting a linear function to pieces of the data bracketing $\sim 0.1 \text{ Å}$ to either side of a given edge, and extrapolate the fit to the expected edge energy (see Fig. 2). (XAFS in the spectrum of GRS 1915+105 are discussed later in this section.) Additionally, since pileup will also affect the depth of an edge by reducing the jump in the discontinuity at the edge, we use the pileup corrected 1st order HEG to assess the optical depth of Fe, S, & Si, and MEG to assess Mg. The column densities (shown in Table 1) are calculated using the value for the K-shell photoionization cross section of the relevant species (⁹ Henke et al., 1993), and evaluated for solar and ISM abundances (Wilms, Allen, McCray 2000). Given the possibility for emission and absorption features and edge structure which we have not accounted for, a conservative estimate for the systematic uncertainties in τ is calculated using the error in the counts and best fit continuum level on either side of the edge to obtain a fractional uncertainty.

⁸<http://space.mit.edu/CXC/ISIS/>

⁹http://www-cxro.lbl.gov/optical_constants/asf.html

TABLE 1
PROMINENT NEUTRAL K EDGES OF THE TIME-AVERAGED DATA

Species	λ_0 (Å)	PHOTOELECTRIC EDGES		
		τ	$^a N_{\text{H}}$ (solar) (10^{22} cm^{-2})	$^b N_{\text{H}}$ (ISM) (10^{22} cm^{-2})
Mg K	9.52	0.29 ± 0.03	$3.1^{+0.3}_{-0.3}$	$4.7^{+0.5}_{-0.5}$
Si K	6.74	0.47 ± 0.01	$8.4^{+0.1}_{-0.1}$	$16.1^{+0.2}_{-0.2}$
S K	5.02	$0.07^{+0.002}_{-0.01}$	$3.2^{+0.1}_{-0.6}$	$4.8^{+0.3}_{-0.9}$
Fe K	1.74	0.11 ± 0.02	$9.3^{+1.6}_{-1.3}$	$10.9^{+1.9}_{-1.5}$

^{a,b} The total hydrogen column assuming (a) solar and (b) ISM abundances. The expected atomic (N_{H}) and molecular (N_{H_2}) hydrogen along the line of sight is respectively $\gtrsim 1.76 \times 10^{22} \text{ cm}^{-2}$ and $\sim 7.43 \times 10^{21} \text{ cm}^{-2}$. The MEG summed 1st order data is used to assess the Mg edge; all other edges were fit using the HEG summed 1st order data.

We compare our results (below) with constraints on the Galactic $^{10} N_{\text{H}_G} \gtrsim 1.8 \times 10^{22} \text{ cm}^{-2}$ (determined from 21 cm emission from atomic hydrogen along the line of sight, Dickey & Lockman, 1990). Despite the corrections for optical depth effects, this value is regarded as a lower limit because of its reduced sensitivity to both cold and ionized H, as well as H_2 . Dame et al. (2001) report additional molecular hydrogen (based on CO maps) with $N_{\text{H}_2} \sim 7.43 \times 10^{21} \text{ cm}^{-2}$ to the nearest l, b towards GRS 1915+105. Therefore, the line of sight column can be $\gtrsim 3 \times 10^{22} \text{ cm}^{-2}$ with contributions from both atomic and molecular hydrogen. (Chapuis and Corbel 2001, in preparation, find the total [atomic plus molecular] line of sight column density toward GRS 1915+105 from millimeter and HI observations to be $3.3 \pm 0.2 \times 10^{22} \text{ cm}^{-2}$; private communication S. Corbel.)

Using the HETG absorption edges for S and Mg, we derive N_{H} values $\sim 3 \times 10^{22} \text{ cm}^{-2}$, assuming solar abundances, and $\sim 5 \times 10^{22} \text{ cm}^{-2}$, assuming ISM abundances. These values are consistent with the N_{H} value derived from low energy continuum absorption. However, the N_{H} derived from Si & Fe (for solar abundances) are greater by $\gtrsim 5 \times 10^{22} \text{ cm}^{-2}$ (and much greater for ISM abundances) when compared with what is expected from the line of sight column density (Table 1). We note that earlier reports by Lee et al. (2001a) for N_{H} were based on data that had not been corrected for pileup.

We point out the exciting possibility that astrophysical XAFS are present in the spectrum of GRS 1915+105, most noticeable in Si, but may also be present at the Mg and Fe edges. XAFS is a general term for both EXAFS (extended X-ray absorption fine structure) and XANES (X-ray absorption near edge structure), with the distinction based on single (EXAFS) versus multiple (XANES) scatterings of the photoelectrons from the immediate neighboring atoms (e.g. Sayers, Stern, & Lytle 1971, Woo, Forrey, & Cho 1997, and references therein). Such features appear as wave-like modulations, with the former manifest in structure at $\gtrsim 50 \text{ eV}$ from the absorption edge, and the latter in the region between the edge and EXAFS region. A qualitative comparison of Si in the detector (SiO_2 and polysilicon) shows that the modulations of the Si EXAFS in our observation are much stronger than that expected from the detectors, and therefore may be features which are associated with the X-ray source. We note further that the detector Si region has been carefully calibrated against ground based measurements at synchrotron beamlines (e.g. Prigozhin et al., 1998; also Mori et

al., 2001 for further studies of absorption edges in front illuminated CCDs). Therefore, we believe that a definitive claim of XAFS in GRS 1915+105 is hampered more by the lack of adequate statistics than calibration errors in the quantum efficiency of the *Chandra* CCDs. (The calibration near the Si edge is good to $\sim 3\%$ over 0.02 Å bins – private communication, H. Marshall.) The possible EXAFS at the Si edge are noted in the instrument-corrected spectrum shown in Fig. 2. An investigation of several slightly less absorbed X-ray binaries which have good statistics and for which the instrumental response was applied (Schulz et al., 2000) do not show XAFS such as that seen here, and gives us further confidence that the XAFS seen in the *Chandra* spectrum of GRS 1915+105 is associated with an astrophysical phenomenon. At present, we merely point out this exciting possibility – an in-depth treatment of XAFS is beyond the scope of this paper, and will be addressed in a subsequent paper which will investigate the presence of XAFS in highly absorbed bright X-ray binaries.

We further verify that the Si edge and possible structure is intrinsic to the source by comparing the measured edge depth against the contribution from the *Chandra* CCDs. The discontinuity in the effective area at the detector Si edge is $\sim 20\text{--}30\%$, and verified to be accurately ¹¹ modeled to $\lesssim 10\%$ but as stated previously can be good to $\sim 3\%$ over 0.02 Å bins; the latter is particularly important for the assurance that the residuals which we attribute to XAFS at the Si edge are not likely to be an instrumental feature. This is compared with the $>$ factor 2 discontinuity measured from the HEG 1st order count spectra. We find further confidence that the Si edge is not a detector feature from the MEG 3rd order spectrum, where the edge remains prominent in the data, but for which there is a minute contribution from the detector. (The spectra for the relevant orders are the combined plus and minus sides; for the MEG 3rd order, the Si edge seen in our spectrum for one of the sides fall on the backside (S1) chip where there is no/little contribution from the detector Si edge. – See e.g. the effective area curves shown in Fig. 2 of Lee et al., 2001a)

5. THE IRON COMPLEX - A HOT DISK ATMOSPHERE ?

In addition to neutral edges, and possible neutral (Fe K α) emission, the spectrum of GRS 1915+105 also exhibits a strong Fe XXVI resonant absorption feature (Fig. 3). A weak Fe XXV resonant absorption may also be present. We detect a $\sim 2.7\sigma$ emission feature at $\sim 1.87 \text{ Å}$ which can be either the Fe XXV $1s^2 1S_0 - 1s2s^3 S_1$ (forbidden) emission, or the emission component of a P-Cygni resonance line of Fe XXV (similar to what is seen in Cir X-1 - Schulz & Brandt, 2001, in preparation). Because the Fe region is $< 5\%$ piled-up, we use the original HEG combined plus and minus 1st order data binned to 0.0075 Å to assess the features detailed in Table 2. The $\sim 0.002 \text{ Å}$ wavelength errors are consistent with the expected accuracy for the HEG data (e.g. §2.1), and present measurements show consistency with a zero velocity shift. (The ASCA spectrum of the microquasar GRO 1655-40 (Ueda et al., 1998) also shows no evidence for blueshifted lines.) The resolution of the *Chandra* HEG is $\sim 1600 \text{ km s}^{-1}$ FWHM ($\sim 10 \text{ mÅ}$) at the iron energies. The velocity widths of Table 2 indicate that the lines are either not resolved or only marginally so. The larger breadth to the line width of the Fe XXVI absorption when compared with

¹⁰<http://heasarc.gsfc.nasa.gov/cgi-bin/Tools/w3nh/w3nh.pl>

¹¹CXC Proposers' Observatory Guide, December 2000, Version 3, p.190

PROMINENT ABSORPTION & EMISSION FEATURES IN THE TIME-AVERAGED DATA

Species	^a λ (Å)	^b λ_{mea} (Å)	^c $\Delta\lambda$ (km s ⁻¹)	^d σ (km s ⁻¹)	^e Flux (10 ⁻³ ph cm ⁻² s ⁻¹)	^e W_{Fe} (mÅ)
Fe XXVI Ly α *	1.7798	1.7752 \pm 0.0024	-770 \pm 400	578 \pm 400	-1.72 \pm 0.41	4.7
Fe XXV Ly α * ¹	1.8505	1.8547 \pm 0.0062	+680 \pm 1000	= Fe XXVI Ly α	-0.61 \pm 0.38	1.7
Fe XXV Ly α	1.8505	1.8540 \pm 0.0070	+570 \pm 1140	499 \pm 728	-0.58 \pm 0.37	1.6
Fe XXV \dagger^1	1.8682	1.8676 \pm 0.0027	-100 \pm 430	= Fe XXVI Ly α	0.98 \pm 0.36	2.7
Fe XXV \dagger	1.8682	1.8685 \pm 0.0028	+50 \pm 450	164 \pm 346	1.00 \pm 0.36	2.7
Fe K α	1.9361	1.9350 \pm 0.0094	-170 \pm 1457	380 \pm 670	-0.71 \pm 0.35	2.0
Un-IDed	—	1.7315 \pm 0.0016	—	177 \pm 165	\lesssim 1.96 \pm 0.51	\lesssim 6
Ca XX Ly α * ²	3.0203	3.0117 \pm 0.0029	-850 \pm 290	205 \pm 135	$>$ 0.34 \pm 0.17	$>$ 1.2

TABLE 2

* Absorption feature; otherwise emission. \dagger Line is identified as either the Fe XXV (f) emission or the emission portion of the Fe XXV (r) P-Cygni. ¹ The line width is tied to that of Fe XXVI absorption. ² Lower limit values quoted since region is heavily piled-up. ^a Rest wavelengths of identified lines from Verner et al., 1995 ^b Best measured centroid wavelengths (Å). ^c Amount of shift of measured wavelength from rest (- for blueshift, + for redshift) ^d 'True' velocity width (km/s). The instrumental line spread function has already been subtracted out. ^e Flux in the line. ^f Equivalent width.

the $\lambda \sim 1.87\text{Å}$ Fe XXV emission (if the forbidden line) may indicate that the region responsible for the Fe XXV emission may only be part of the region responsible for the Fe XXVI absorption. Alternatively, the $\lambda \sim 1.87\text{Å}$ line is the (r) emission component of the Fe XXV P-Cygni complex which is equally divided between absorption and emission.

Because the Fe XXVI and Fe XXV resonant absorption features are detected, we can estimate the physical parameters of the plasma from which they originate based on the ratio of the Fe XXVI : Fe XXV column densities ($N_{\text{Fe26}} : N_{\text{Fe25}}$). If the lines are resolved (e.g. Fe XXVI), we can assume that they are unsaturated and on the linear part of the curve of growth, and therefore estimate the Fe XXVI and Fe XXV column densities to be $N_{\text{Fe26}} \sim 4 \times 10^{17} \text{ cm}^{-2}$ and $N_{\text{Fe25}} \sim 7 \times 10^{16} \text{ cm}^{-2}$ based on the relation

$$\frac{W_\lambda}{\lambda} = \frac{\pi e^2}{m_e c^2} N_j \lambda f_{ij} = 8.85 \times 10^{-13} N_j \lambda f_{ij} \quad (1)$$

where N_j is the column density for the relevant species, f_{ij} (respectively for Fe (XXV, XXVI) is 0.798, 0.416, from Verner 1995) is the oscillator strength, W_λ is the equivalent width of the line, and λ is the wavelength in cm units (Spitzer 1978). (If instead, the features are due to a superposition of saturated lines over a range of velocities, the column densities quoted would be higher.) The 1σ confidence upper limit for the Fe XXV flux in Table 2 gives an equivalent width $\sim 2.7 \text{ mÅ}$, and therefore $N_{\text{Fe25}} \lesssim 1.1 \times 10^{17} \text{ cm}^{-2}$ (compared with the bestfit $N_{\text{Fe25}} \sim 7 \times 10^{16} \text{ cm}^{-2}$ quoted above). We use this upper limit value of N_{Fe25} for our subsequent calculations to estimate the physical conditions (e.g. temperature, ionization parameter, etc.) of the hot plasma. Results based on calculations using the best-fit Fe XXV flux and equivalent width will be noted in '[]'.

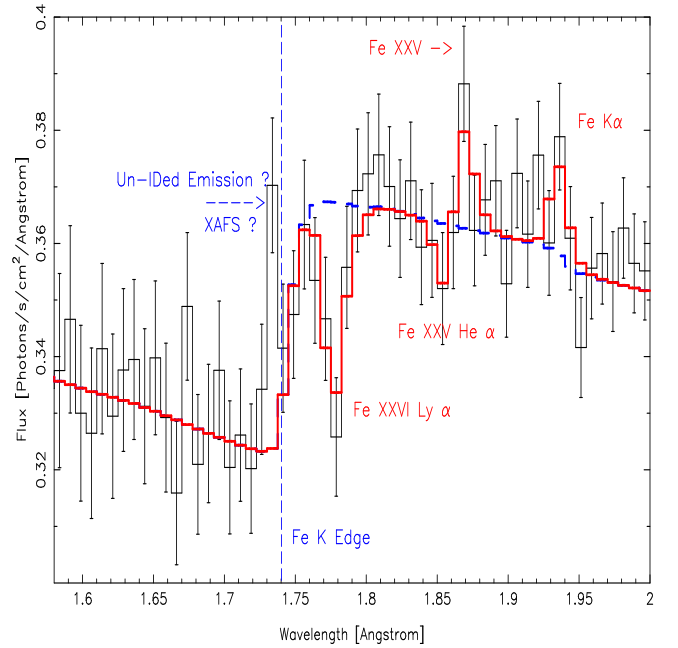


FIG. 3.— Time-averaged AO1 30ks HEG 1st order data of the Fe region binned to 0.0075 Å show both ionized (most likely from the accretion disk atmosphere) and neutral (from the source environment, or along the line of sight) Fe features. Over-plotted is the best fit continuum (dashed blue) and identified (red) lines. The unidentified line may be a shift in the edge due to XAFS.

Based on the calculations of Kallman & Bautista (2001) for a power law ionizing spectrum of energy index $\alpha = -1$ ($\Gamma = 2$), and photoionized plasma, the ratio of N_{Fe26} to N_{Fe25} implies an ionization fraction of $\lesssim 0.45$ [~ 0.39] for Fe XXVI from which we estimate $\log \xi \gtrsim 4.15$ [erg cm s⁻¹] [$\log \xi \sim 4.3$], and $T \gtrsim 2.4 \times 10^6 \text{ K}$ [$\sim 2.7 \times 10^6 \text{ K}$]. (This is a much higher ionization state than that reported by Kotani et al., 2000 for their high temperature limit.) Given the likelihood that these ionized features originate in close proximity to the bright X-ray source, we expect photoionization (rather than collisional ionization) to be the dominant physical process, due to the high radiation field. (Temperatures of $\gtrsim 10^8 \text{ K}$ would be necessary for producing hydrogen-like iron in a collisionally ion-

ized plasma.) We next correct for the ionization fraction to obtain an equivalent hydrogen column N_H in this region respectively for solar and ISM abundances to be $2.8 \times 10^{22} \text{ cm}^{-2}$ and $3.3 \times 10^{22} \text{ cm}^{-2}$. Based on the relation $\xi = L/nR^2 \text{ erg cm s}^{-1}$ where $N_H = n\Delta R \equiv$ the maximum column density in this region, we estimate $R^2/\Delta R \sim 2 \times 10^{12} \text{ cm}$. (R is defined to be the distance from the ionizing flux to the absorber and ΔR the thickness of the absorber.) If we further postulate that the volume filling factor $\Delta R/R$ must be small (e.g. ≈ 0.1) in order that ξ not change over the region, we estimate an upper limit on $R \lesssim 2 \times 10^{11} \text{ cm}$, implying that $\Delta R \approx 2 \times 10^{10} \text{ cm}$. It follows that the hydrogen equivalent number density $n \gtrsim 2 \times 10^{12} \text{ cm}^{-3}$ (assuming solar abundances).

It is plausible that the ionized absorber responsible for the H- and He-like Fe lines at a distance $R \lesssim 10^{11} \text{ cm}$ is associated with material flowing out from the X-ray source (e.g. wind, see also §6), which we can compare with the accretion rate. Using the relation for the ionization parameter, we can define the (spherical) mass outflow rate \dot{M}_{flow} at a velocity $v \sim 10^7 \text{ cm s}^{-1}$ (100 km s^{-1}) to be

$$\dot{M}_{flow} = 4\pi r^2 n m_p v \left(\frac{\Omega}{4\pi}\right) = 4\pi m_p v \left(\frac{L_x}{\xi}\right) \left(\frac{\Omega}{4\pi}\right) \quad (2)$$

$$\sim 9.5 \times 10^{18} \left(\frac{\Omega}{4\pi}\right) \text{ gm s}^{-1}$$

where r is the characteristic radius, $\rho = n m_p$ is the density of the absorbing material, with n equal to the number density of electrons in this material and m_p the proton mass, and $\Omega \equiv$ solid angle subtended by the outflow. This can be contrasted with

$$\dot{M}_{accretion} = \frac{L_{bol}}{\eta c^2} \sim 7.1 \times 10^{18} \text{ gm s}^{-1} \quad (3)$$

where the efficiency $\eta \sim 0.1$ and the lower limit on the bolometric luminosity $L_{bol} \sim L_x$ is used. (from §3). Such a comparison for $v \sim 100 \text{ km s}^{-1}$ shows that as the covering fraction (i.e. $\Omega/4\pi$) approaches unity, the mass flux in the flow (or wind) can be comparable to that in the disk.

The high ionization state of the hot medium (even based on the lower limit $\log \xi \sim 4.15$) which supports the H- and He-like Fe lines is too ionized to support most other species with the exception of H-like Ar XVIII (ionization fraction $\sim 9\%$) and H-like Ca XX ($\sim 16\%$), and Fe XXV ($\sim 12\%$), compared to the $\sim 45\%$ ionization fraction for Fe XXVI. (These percentages will decrease with increasing ionization.) The lower limit (since this region is severely affected by pileup) to the column density of Ca XX ($f_{ij} = 0.416$) is $N_{Ca20} \gtrsim 3.6 \times 10^{16} \text{ cm}^{-2}$

6. TRACKING VARIABILITY IN THE DISK ?

The count rates from the *Chandra* HETGS and the *RXTE* PCA instruments for GRS 1915+105 are shown in the top two panels of Fig. 4a. To investigate the physical processes which may be related to the observed temporal variability, we use the PCA spectral parameters to compute the inferred bolometric flux from the accretion disk (Fig. 4a, panel 3) and from the power law component (1-20 keV; panel 4). We find that the most significant variations occur in the disk blackbody component, although there is also a smaller dip in the power-law flux as well.

The time-sliced *Chandra* data shown in Fig. 4b suggests that evolution of the ionized line features may also be correlated with changes to the disk flux. In particular, the *Chandra* spectra shows that the Fe XXV line is more prominent during the dip between the ~ 10 – 20 ks of our observation, in contrast to the

prominence of the Fe XXVI absorption at the beginning and end of the observation when the source is brighter. The time interval corresponding to the strongest Fe XXV absorption is coincident with the dip in the Fig. 4a (panels 1 & 2) light curve count rate, as well as the notable diminution of the disk flux (panel 3), and to a lesser extent, the power law flux (panel 4) seen in the *RXTE* data. This would support the idea that the ionized absorption features originate from the disk. However, we note that an $\sim 20\%$ change in the flux at the ionization discussed in §5 implies an $\sim 30\%$ change in the ionization fraction of Fe XXV, if we assume that ξ scales with the ionizing flux, while n and R remain constant. This is not sufficient to explain the lack of Fe XXV absorption, and dominance of Fe XXVI absorption during the periods when the count rate is high. An $\sim 50\%$ change in ξ which will reduce the ionizing fraction of Fe XXV by a factor of two might be more plausible for explaining what is observed, indicating that the ionizing flux is only part of the solution, and changing density the other factor. If we consider the calculations in §5 for a wind with velocity $v \sim 10^7 \text{ cm s}^{-1}$ and distance to the absorber $R \sim 10^{11} \text{ cm}$, it is plausible that the spectral variability can be attributed to a flow which can change on timescales of 10 ks such as that seen here. This is not inconceivable since 10 ks is a very long time, corresponding to many dynamical timescales of the relevant parts of the disk, in the life of a source like GRS 1915+105. Furthermore, since this source accretes near its Eddington limit, one would expect the mass flow rate and wind density to be strong functions of the luminosity, such that the actual structure of the wind (i.e. density and size) can change as a function of the luminosity. Similarly observed variations in Cir X-1 have been interpreted to be due to changes in the ionization fraction of the wind (Schulz & Brandt, 2001, in preparation). We note however that the statistics are not adequate for us to present a complete quantitative picture for GRS 1915+105, especially in light of the numerous problems we have with pileup that need to be considered. Cycle 2 *Chandra* data of GRS 1915+105 taken in a mode that optimally reduces pileup will be able to study the variability aspects in greater detail.

7. DISCUSSION

The *Chandra* HETGS spectrum of GRS 1915+105 shows neutral and ionized features superposed on a continuum best described by a disk blackbody and a dominating power-law modified by a column of $\sim 5 \times 10^{22} \text{ cm}^{-2}$ absorption. The X-ray spectral and temporal characteristics as well as the 3.7 Hz QPO seen in our data, and the detection of faint radio emission are all consistent with the low-hard state. This indicates that the X-ray power-law is the dominant emission component and there is a weak and persistent radio jet. No obvious red- / blue-shifted features indicative of a jet can be seen in the time-averaged *Chandra* spectrum.

The H column density derived from the Si and Fe edges (assuming solar abundances) is ~ 8 – $9 \times 10^{22} \text{ cm}^{-2}$, which is substantially higher than the values derived from S and Mg, and continuum absorption determined from broad-band instruments. The discrepancy for excess Si and Fe absorption is even higher if we assume ISM abundances.

There is a possibility that the high X-ray column density and abundance excesses may be related to material that is associated with the immediate environment of the source. Both Mirabel et al. (1996) and Martí et al. (2000) have suggested the possibility for heated dust that is associated with the surroundings of

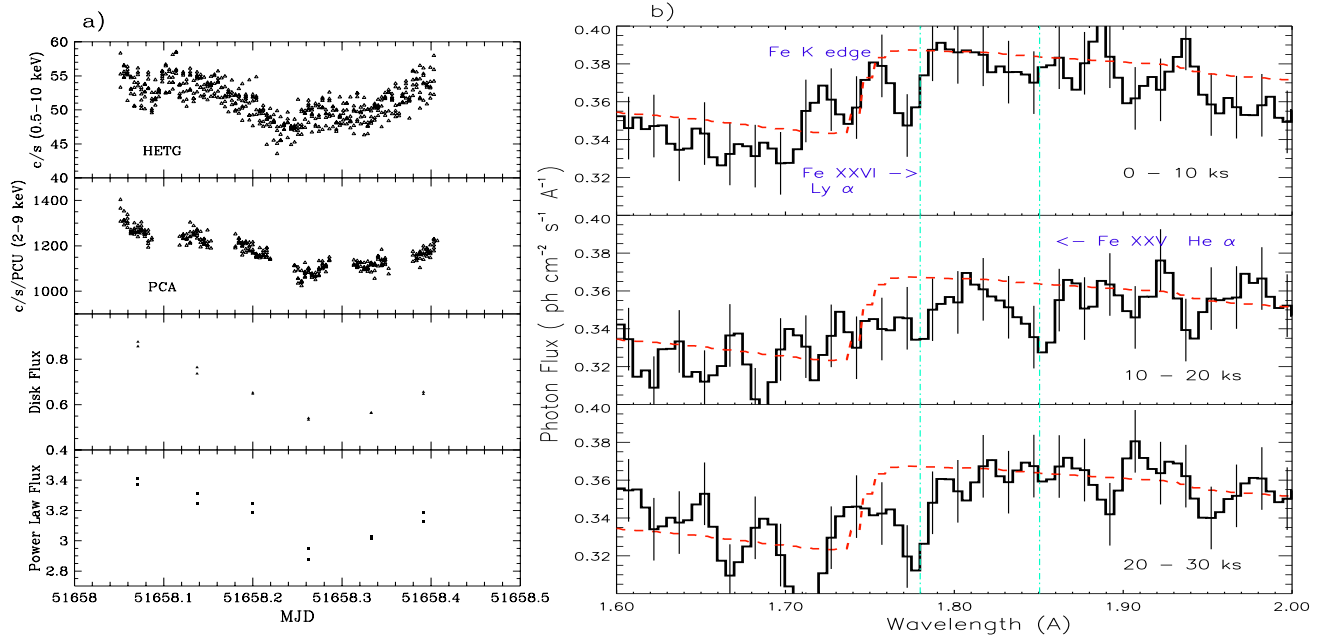


FIG. 4.— (a) Simultaneous *Chandra* (top panel 1) and *RXTE* (panel 2) light curves during the epoch beginning 2000 April 24 at 01:35:49 (MJD: 51658.06654). Changes in the blackbody flux (panel 3) and power-law flux (panel 4) are coincident with changes in the light curve count rates. (Panels 3 & 4 are in units of $10^{-8} \text{ erg cm}^{-2} \text{ s}^{-1}$.) (b) The 30 ks *Chandra* spectrum divided into three 10 ks intervals depicts the evolution of the spectral features. Note in particular the prominence of the Fe XXVI absorption at the beginning and end of the observation when the flux was highest, and of Fe XXV during the dip. Over-plotted is the rough shape of the continuum (red-dashed) from the time-averaged spectra shown in Fig. 3. Error bars are representative of a statistically independent bin for which the data have been boxcar smoothed by 3, corresponding to $\sim 0.0075 \text{ \AA}$.

GRS 1915+105 from IR observations. If true, these anomalous Si and Fe abundances may provide hints to the evolutionary events which gave rise to this source, and the black hole in particular. However, we acknowledge that more data from other X-ray binaries with similar galactic column densities are necessary to determine the absorption abundance ratios over the Galaxy and so confirm that the results for GRS 1915+105 are exceptional. Thus far, observations of SS 433 (Marshall et al. 2001) and Cyg X-1 (Schulz et al. 2001) do not show such Fe and Si overabundances. (See also e.g. respectively Paerels et al. 2001 and Schulz et al. 2001 for the X-ray binaries X0614+091 and Cyg X-1, and Lee et al. 2001b for the extragalactic source MCG-6-30-15.) Clearly, further sensitive measurements such as these of photoelectric edges with *Chandra* will provide valuable information for assessing the material which surrounds bright X-ray sources especially if depletion plays a prominent role. Such measurements will be particularly important for confirming the tentative detection of XAFS (particularly in Si) as reported here. If true, such a positive detection of these absorption fine structure representative of material in solids (as e.g. interstellar grains) will have important consequences for conducting solid state astrophysics, by which grain properties can be extracted via the solid's inner compound structure.

In the interim, the abundance excesses for X-ray absorption edges in GRS 1915+105 can be contrasted with the discovery of abundance anomalies in the optical spectra of companion stars in the microquasars GRO J1655-40 and V4641 Sgr (Israelian et al. 1999; Brown et al. 2000; Orosz et al. 2001). In the latter cases, the over-abundances of α -process elements, but not the Fe group, has led to the hypothesis that the companion star captured supernova or hypernova ejecta is related to the formation

of the black hole. The Fe in the progenitor's core is likely to be efficiently captured by the black hole. In the case of GRS 1915+105, the Fe and Si overabundance pertains to material along the line of sight, and the enrichment may signify either a highly unusual supernova or perhaps external supernova activity local to the binary.

One way to reconcile the overabundance of Fe in GRS 1915+105 is if an asymmetric hypernovae/supernova explosion produced heavier elements like Fe and Si along the poles. For the $14M_{\odot}$ black hole in GRS 1915+105, the binary spin axis would then have to be misaligned with the 70° inclination of the jet (Mirabel & Rodríguez 1994) with respect to the line of sight. Such a misalignment could be induced by disk warping, precession of the spin axes, or residual angular momentum from the initial supernova explosion.

One rather speculative possibility is that the excess Fe and Si might indicate a connection between some kind of SN and BH microquasars. Given that BH microquasars are likely formed from SN, Gamma-ray bursts (GRB) may also represent some kind of microquasar (e.g. Blackman et al. 1996; Kouveliotou et al. 1999) formed similarly (Paczynski 1998; Brown et al. 2000). This makes contact with the results of Brown et al. (2000) for GRO 1655+40, although as mentioned above, there the overabundant elements are α -process elements S and O which are more easily understandable as a SN signature. Nevertheless, one might ultimately imagine a classification of microquasars analogous to that of AGN.

In addition to the first detection of photoelectric edges in GRS 1915+105, our *Chandra* observation confirms the presence of absorption features from highly ionized gas previously reported by Kotani et al. (2000) with *ASCA* data taken between

in 1994 to 1999. Despite their use of a very complicated continuum model, it is evident from Fig. 1 of Kotani et al. (2000) that the observations showing strong absorption features (years 1994 and 1995) display steep X-ray spectra near 10 keV, in contrast with the 1996 observation, where the spectrum is harder, and no absorption features were found with the *ASCA* data. We confirm with the *RXTE* PCA data archive that GRS1915+105 was in a bright mode (1.2 Crab) of the hard-steady state on 1996 October 23 (see Muno et al. 2001). One might therefore suspect from the reported *ASCA* observations that the absorption features from highly ionized atoms are confined to the soft X-ray states of GRS 1915+105; however, the *Chandra* results shown here clearly show such absorption features in the low-hard state (0.4 Crab), as well. This is consistent with the view that the absorbing gas is associated with the accretion disk, which appears evident as the soft component in the X-ray spectrum.

Given that GRS 1915+105 is probably accreting near or above its Eddington limit, the presence of a strong radiatively-driven wind is almost expected. However, we do not find obvious P-Cygni profiles attributed to a disk wind — i.e., redshifted/rest-frame emission lines (from material out of the line of sight) accompanied by blueshifted absorption lines (from the foreground, line-of-sight parts of the wind) in the time-averaged data, akin to what has been reported for Cir X-1 (Brandt & Schulz 2000). The lack of a wind from the star may corroborate the finding that the donor in GRS 1915+105 is a LMXB (Greiner et al., 2001a) where accretion via Roche lobe overflow is the most plausible mechanism for mass transfer. However, the wind (and/or jet signatures) if present (e.g. §5) in GRS 1915+105 is likely to originate from the disk, and may show up in a more subtle form (e.g. through variability studies, §6). The ionized Fe absorption lines of the time averaged spectrum are likely to have origins from the disk or disk atmosphere.

This hot absorbing medium is a particularly important topic, since it points to a disk atmosphere, and possibly even disk wind, or some other type of hot gas structure that is absent from most models for black hole accretion. It will be interesting to diagnose the effects of scattering and absorption in

this medium with *Chandra* spectra of GRS 1915+105 in different flux states, in order to build a picture of which spectral changes are inherent to the source and which are tied to changes along the line of sight to the source. The latter topic is a highly controversial one for GRS 1915+105. The violent changes seen in the apparent disk radius and temperature have been interpreted on some occasions as physical changes that represent the disk instability (Belloni et al 1997) and the effects of the jet production mechanism (Eikenberry et al. 1998). However, analogous disk changes, particularly when the variations are more modest, have been alternatively interpreted as effects due to radiative transfer in an accretion disk (Merloni Fabian & Ross 2000). The *Chandra* spectra (§6) suggest that the apparent changes in the strength of the Fe XXV and Fe XXVI absorption can be linked to changes in the incident ionizing flux and density, and may point to a flow which can change over ~ 10 ks time scales. Clearly, longer continuous observations with *Chandra* and *RXTE* are needed for this source in order to monitor the observed variability, and differentiate between the different mechanisms which may be responsible.

ACKNOWLEDGMENTS

We wish to thank John Houck for assistance with ISIS, Claude Canizares for critical discussions and useful suggestions, and John Davis for expert advice on pileup correction. We also thank Thomas Dame for advice on the interpretation of line of sight column densities, Tim Kallman, Frits Paerels, Jörn Wilms, Anil Pradhan and Justin Oelgoetz for advice. We also thank many of our colleagues in the MIT HETG/CXC group, and acknowledge the great efforts of the many people who contributed to the *Chandra* program. This work was funded by the Chandra grant GO0-1103X. JCL also acknowledge support from the NASA contract NAS8-39073, and NSS from SAO SV1-61010. CSR acknowledges support from Hubble Fellowship grant HF-01113.01-98A — this grant was awarded by the Space Telescope Institute, which is operated by the Association of Universities for Research in Astronomy, Inc., for NASA under contract NAS 5-26555. ACF thanks the Royal Society for support.

REFERENCES

- Belloni, R., Méndez, M., King, A.R., van der Klis, M., van Paradijs, J., 1997, *ApJ*, 488, L109
 Blackman, E. G., Yi, I., & Field, G. B. 1996, *ApJ*, 473, L79
 Brandt, W.N., N.S., Schulz N.S., 2000, *ApJ*, 544, L123
 Brown, G. E., Lee, C.-H., Wijers, R. A. M. J., Lee, H. K., Israelian, G., & Bethe, H. A. 2000, *New Astronomy*, 5, 191
 Castro-Tirado, A. J., Brandt, S., & Lund, N. 1992, *IAU Circ.*, 5590, 2
 Castro-Tirado, A.J., Geballe, T.R., Lund, N., 1996, 461, L99
 Daltabuit E., Cox D.P., 1972, *ApJ*, 177, 855
 Dame, T.M., Hartmann, D., Thaddeus, P., 2001, *ApJ*, 547, 792
 Davis, J.E., 2001, *ApJ*, in press
 Dhawan, B., Mirabel, I.R., & Rodríguez, L.F., 2000, *ApJ*, 543, 373
 Dickey, J.M., & Lockman, F.J., 1990, *ARAA*, 28, p215
 Eikenberry, S.S., Matthews, K., Morgan, E.H., Remillard, R.A., Nelson, R.W., 1998, *ApJ*, 494, L61
 Greiner, J., Cuby, J. G., McCaughrean, M. J., Castro-Tirado, A. J., & Mennickent, R. E. 2001a, *A&A*, 373, L37
 Greiner J., McCaughrean M.J., Cuby J.G., 2001b, *Nature*, in press
 Henke, B. L., Gullikson, E. M., & Davis, J. C., 1993, *At. Data Nucl. Data Tables*, 54, 18
 Houck, J.C., & DeNicola, L.A., 2000, *ASP Conf. Ser.*, Vol 216, 591
 Israelian, G., Rebolo, R., Basri, G., Casares, J., Martin, E.L., Nat., 401, 142
 Jahoda K., Swank, J.H., Giles, A.B., Stark, M.J., Strohmayer, T., Zhang, W., 1996, *Proc. SPIE*, 2808, "EUV and Gamma Ray Instrumentation for Astronomy", VII, 59
 Kallman, T. R., & Bautista, M., 2001, *ApJ Supp*, 133, 221
 Kotani, T., Ebisawa, K., Dotani, T., Inoue, H., Nagase, F., Tanaka, Y., Ueda, Y., *ApJ*, 2000, *ApJ*, 539, 413
 Kouveliotou, C. et al. 1999, *ApJ*, 510, L115
 Lee J. C., Ogle P.M., Canizares C.R., Marshall H.L., Schulz N.S., Morales R., Fabian A.C., Iwasawa I., 2001b, *ApJ*, 554, L13
 Lee J. C., Schulz N.S., Reynolds C. S., Fabian A. C., Blackman E.G., 2001a, 'X-ray Astronomy 2000', Eds. R. Giacconi, L. Stella and S. Serio, *ASP Conference Proceedings*, in press, (astro-ph/0012111)
 Marshall, H.L., Canizares, C.R., and Schulz, N.S., 2001, *ApJ*, submitted
 Martí J., Mirabel I.F., Chaty S., Rodríguez L.C., 2000, *A&A*, 356, 943
 Merloni, A., Fabian, A.C., Ross, R.R., 2000, *MNRAS*, 313, 183
 Mirabel, I.F., Rodríguez, L.F., 1999, *Annual Review of Astronomy and Astrophysics*, 37, 409
 Mirabel I. F., Rodríguez L. F., 1994, *Nature*, 371, 46
 Mirabel, I.F., Rodríguez, L.F., Chaty, S., Sauvage, J., Gerard, E., Duc, P.A., Castro-Tirado, A.L., Callanan, P., 1996, *ApJ*, 472, L111
 Morgan, E.H., Remillard, R.A., Greiner, J., 1997, *ApJ*, 482, 993
 Mori, K., et al., 2001, *Nucl. Inst. & Methods in Phy. Research A*, 459, 191
 Muno, M.P., Morgan, E.H., Remillard, R.A., 1999, *ApJ*, 527, 321
 Muno, M.P., Remillard, R.A., Morgan, E.H., Waltman, E.B., Dhawan, V., Hjellming, R.M., Pooley, G., 2001, in press (astro-ph/0104067)
 Oelgoetz, J., & Pradhan, A. K., 2001, *MNRAS*, submitted (astro-ph/0106330)
 Orosz, J. A., Kuulkers, E., van der Klis, M., McClintock, J. E., Garcia, M. R., Callanan, P. J., Bailyn, C. D., Jain, R. K., & Remillard, R. A. 2001, *ApJ*, submitted; astro-ph/0103045
 Paczynski, B. 1998, *ApJ*, 494, L45
 Paerels, F., Brinkman, A.C., van der Meer R.I.J., et al., 2001, *ApJ*, 546, 338

- Prigozhin, G., Woo, J., Gregory, J., Loomis, A., Bautz, M., Ricker, G., Kraft, S., 1998, *Optical Engineering*, vol. 37, No. 10, pp. 2848
- Rothschild, R. E., et al., 1998, *ApJ*, 496, 538
- Sayers, D.E., Stern, E.A., & Lytle F., 1971, *Phys. Rev. Lett.*, 27, 1204
- Schulz, N.S., Cui, W., Canizares, C.R., Marshall, H.L., Lee, J.C. , Miller, J.M., Lewin, W.H.G., 2001, *ApJ*, submitted
- Schulz, N. S., Marshall, H. L., Levine, A., Cui, W., Dewey, D., & Canizares, C. R. 2000, *American Astronomical Society Meeting*, 196, 3419
- Spitzer, L. 1978, New York, Wiley-Interscience, 1978, p.52
- Ueda, Y., Inoue, H., Tanaka, Y., Ebisawa, K., Nagase, F., Kotani, T., Gehrels, N., 1998, *ApJ*, 492, 782, (erratum 500, 1069)
- Verner, D. A. & Yakovlev, D. G. 1995, *A&AS*, 109, 125
- Wilms J., Allen A., McCray R., 2000, *ApJ*, 542, 914
- Woo, J.W., Forrey, R.C., Cho, K., 1997, *ApJ*, 477, 235